Voltage-Driven Instability of Electrically Conducting Fluids

Egbert Zienicke[1], Norbert Seehafer[2], Ben-Wen Li[3,1], Jörg Schumacher[4], Hélène Politano[5], and André Thess[1]

[1] Fakultät Maschinenbau, Technische Universität Ilmenau, PF 100565, 98684 Ilmenau, Germany
[2] Institut für Physik, Universität Potsdam, PF 601553, 14415 Potsdam, Germany
[3] Thermal Engineering Department, School of Materials and Metallurgy, Northeastern University, Shenyang Liaoning 110004, China
[4] Department of Mechanical Engineering, Yale University, P.O. Box 208284, New Haven, CT 06520-8284, USA
[5] Observatoire de la Côte d'Azur, CNRS, B.P. 4229, 06304 Nice Cedex 4, France

Summary

This paper consists of two parts dealing with magnetohydrodynamic pinch instabilities in cylindrical and in planar geometry.
The first part of the paper gives a plot for a spectral code in cylindrical geometry that is able to simulate the magnetohydrodynamic (MHD) approximation for very small magnetic Reynolds and Prandtl numbers. The approximated set of evolution equations is appropriate for the fluid behaviour of liquid metals on a laboratory scale under the influence of external and internal magnetic fields. The geometry and the MHD model require the development of a spectral Poisson solver for an expansion partly in Fourier series (axial and azimuthal directions) and partly in Chebyshev polynomials (radial direction). The cylindrical code will be used for the computation of the bifurcation sequence inside a cylindrical cavity filled with liquid metal.
In the second part results for the plane sheet pinch are presented which were obtained using a pseudo-spectral code with Fourier expansions in the three Cartesian coordinates. The planar case involves a space-dependent resistivity: for a given profile of the resistivity a numerical stability and bifurcation analysis is carried out on the basis of the full MHD equations. The most unstable perturbation to the quiescent basic state is the two-dimensional tearing mode. Restricting the whole problem to two spatial dimensions, this mode was followed up to a time-asymptotic steady state, which however proved to be unstable to three-dimensional perturbations even close to the point where the primary instability sets in. For a special choice of the system parameters, the unstably perturbed state was followed up in its nonlinear evolution and was found to approach a three-dimensional steady state.

1 Introduction

Pinch instabilities appear in a variety of circumstances in electrically conducting fluids, for example in plasmas and in liquid metals. In the applicaton of controlled

nuclear fusion the pinch effect is rather undesirable because it prohibits confinement of hot plasma by using magnetic fields, and one has to find ways to suppress the pinch instability.

The physical mechanism of the pinch effect can be understood easily in a cylindrical geometry. Suppose an electric current with density $\mathbf{J_0}$ is flowing in the axial direction through a fluid conductor of cylindrical shape. According to the right-hand rule, this axial current generates an azimuthal magnetic field $\mathbf{B_0}$ with field lines closing around the axis of the cylinder. Inside the fluid the current and its magnetic field give rise to a Lorentz force $\mathbf{J}_0 \times \mathbf{B}_0$ directed towards the cylinder axis. This force allows the confinement of plasma without walls as long as it is in equilibrium with the static pressure of the fluid. The equilibrium state is, however, unstable to perturbations involving rotationally symmetric fluid displacements that vary along the axis. Such perturbations can grow exponentially by the so-called 'sausage instability', which tries to pinch off the fluid column. The sausage instability can be used in electrical engineering to build liquid metal switches which are able to cut off short circuits on timescales of a few milliseconds (see [21]).

Linear stability analysis and experiments in fusion research have shown that there exist also pinch instabilities which are not rotationally symmetric [1]. They are named kink instabilities and can be characterized by azimuthal wavenumbers $m = 1, 2 \ldots$ (the sausage instability has wavenumber $m = 0$). For the kink instabilities the current density assumes a helical structure and the Lorentz force drives a fluid motion with m helical vortices. The sausage instability is normally most easily excited, i.e. it occurs at a smaller imposed current density than the kink instability with $m = 1$. But if one assumes that an incompressible fluid (like a liquid metal) is enclosed in a cylindrical volume with rigid boundary, the sausage instability cannot occur due to mass conservation. In this case the $m = 1$ kink instability is the first instability that can be observed for increasing current density. Different from the sausage instability, it can lead to a stationary flow pattern of two helical vortices inside the cylindrical fluid volume, as shown by Montgomery et al. [4, 20] using the full magnetohydrodynamic (MHD) equations. The critical parameter for this bifurcation to magnetoconvection is the Hartmann number Ha (see [11]). Ha is the geometric mean of two Reynolds-like numbers, one being kinetic and the other magnetic. These do not influence the stability boundaries independently, but only combined in the Hartmann number.

Also in a planar geometry one can in principle expect pinch instabilities. In this case one considers a sheet or a layer of fluid as shown in Fig. 1 . The layer is bounded by two planes parallel to the x_2-x_3 plane; it is infinitely extended in the x_2 and x_3 directions and has a finite thickness L_1. One assumes an electric current flowing in the x_3 direction which generates a magnetic field parallel to the x_2 axis, with a direction reversal (i.e. $B_2 = 0$) in the midplane of the layer. If the bounding planes are free surfaces of liquid metal a sausage-like instability can be expected. Considering the side walls as fixed and the fluid as incompressible, the sausage instability is suppressed and a kink-like instability can be expected, driving a flow in the form of straight convection rolls on both sides of the midplane.

Our principal goal is to investigate the bifurcation sequence of a liquid metal inside a cylindrical cavity traversed by an axial current. After the first bifurcation to the helical convection state observed by Montgomery et al. further bifurcations are expected that lead to time-dependent states with flow and eventually to turbulence. As liquid metals have very small magnetic Prandtl numbers (the magnetic Prandtl number is the ratio between kinematic viscosity and magnetic diffusivity) and on laboratory scales the magnetic Reynolds numbers are normally also very small, a quasistatic approximation can be used for the electromagnetic quantities. In Section 2 we describe a numerical code based on spectral methods that is able to solve the approximated set of equations. While the cylindrical code is still under construction, we used an already existing code for the computationally simpler Cartesian geometry to investigate the bifurcation in the planar case. As described in Section 3, the planar case and the cylindrical case do not behave completely the same way. Different from the cylindrical case, in the planar geometry an instability appears only for space dependent resistivity. The reason is that only for appropriately varying resistivity the profile of the equilibrium magnetic field (i.e. of the field component B_2) across the sheet becomes such as to allow instability. In the cylindrical case such unstable profiles (in the radial direction) already result from geometric effects. That is to say, the cross-sheet variation of the resistivity in the planar case leads to similar effects as the curvature of the magnetic field lines in the cylindrical case. We start our calculations from the Harris equilibrium for a plane sheet and compute its stability boundaries as well as 2D and 3D time-asymptotic states after the bifurcation has taken place.

2 Kink instability for liquid metal in a cylindrical cavity

2.1 MHD equations for liquid metal

There are metals which are in the liquid state for room temperatures, for example mercury or an alloy of sodium and potassium, which was used by Northrup for his pinch experiment [12]. In the last years an alloy of gallium, indium and tin has been used more and more for MHD experiments and applications (for example the liquid metal switch). It has the advantage to be much less toxic than mercury and much less reactive chemically than sodium and potassium. Experiments to measure the flow caused by the kink instability in a cylindrical container will in general be easier with GaInSn than using a plasma. On the other hand, because of the low magnetic Prandtl numbers of liquid metals the appearance and properties of the instability can be different from the plasma physics case. As the behaviour of liquid metals carrying electric currents is basic to many material processing devices, the pinch effect in liquid metals is an interesting and important subject on its own.

From the point of view of numerical MHD simulation for liquid metals, the very small magnetic Prandtl numbers, $Pr^M = 10^{-5} \ldots 10^{-6}$, represent a serious problem. The diffusive timescales of the magnetic field and the flow differ by a factor of at least 10^5, which results in the difficulty that very small timesteps are needed to solve the Navier-Stokes equation and the induction equation in parallel. Therefore an

approximation has been developed which is appropriate for the numerical study of liquid metals. It works for lengthscales of laboratory experiments, where the magnetic Reynolds number can be considered as small, $Re^M \ll 1$. For small magnetic Prandtl and Reynolds numbers we now describe a quasistatic approximation to the induction equation.

It is useful to split the current density $\mathbf{J}$ and the magnetic field $\mathbf{B}$ into externally applied and induced parts,

$$\mathbf{J} = \mathbf{J}_0 + \mathbf{j}, \qquad \mathbf{B} = \mathbf{B}_0 + \mathbf{b}\,, \tag{1}$$

where the index 0 refers to externally applied quantities. In fact, the magnetic Reynolds number is a measure of the strength of the induced fields:

$$\frac{|\mathbf{b}|}{|\mathbf{B}_0|} \approx \frac{|\mathbf{j}|}{|\mathbf{J}_0|} \approx Re^M \tag{2}$$

We now consider a cylinder of radius R filled with a liquid metal through which an externally driven, axially directed current of homogenous density is flowing. The cylinder axis is taken as the z axis in a system of cylindrical polar coordinates r, φ, z:

$$\mathbf{J}_0 = j_0 \mathbf{e}_z \tag{3}$$

$$\mathbf{B}_0 = \frac{\mu_0 j_0}{2} r \mathbf{e}_\varphi + \hat{B}\mathbf{e}_z\,, \tag{4}$$

where $\mathbf{e}_z$ and $\mathbf{e}_\varphi$ are unit vectors in the axial and azimuthal directions and μ_0 is the vacuum magnetic permeability. The first term on the right of Eq. (4) is the magnetic field that is generated by the homogenous current density $j_0\mathbf{e}_z$ inside the fluid volume, while the second term corresponds to a homogenous field applied externally (i.e. the currents generating the field $\hat{B}\mathbf{e}_z$ flow outside the fluid volume).

We use the nonrelativistic, incompressible MHD equations,

$$\rho\left(\frac{\partial \mathbf{v}}{\partial t} + (\mathbf{v}\cdot\nabla)\mathbf{v}\right) = \rho\nu\nabla^2\mathbf{v} - \nabla p + \mathbf{J}\times\mathbf{B}, \tag{5}$$

$$\frac{\partial \mathbf{B}}{\partial t} = \nabla\times(\mathbf{v}\times\mathbf{B}) + \eta\nabla^2\mathbf{B}, \tag{6}$$

$$\nabla\cdot\mathbf{v} = 0, \quad \nabla\cdot\mathbf{B} = 0, \tag{7}$$

where $\mathbf{v}$ is the fluid velocity, ρ the mass density, p the thermal pressure, ν the kinematic viscosity, and η the magnetic diffusivity, which is connected with the electrical conductivity σ by the relation $\eta = 1/\mu_0\sigma$. The electric current density is not an independent variable but given by $\mathbf{J} = \nabla\times\mathbf{B}/\mu_0$. Inserting (1) into the induction equation, Eq. (6), and taking into account that for our problem $\mathbf{B}_0$ is time-independent and $\nabla^2\mathbf{B}_0$ is zero, one gets the following equation for the time evolution of the induced magnetic field:

$$\frac{\partial \mathbf{b}}{\partial t} = \nabla\times(\mathbf{v}\times(\mathbf{B}_0 + \mathbf{b})) + \eta\nabla^2\mathbf{b} \tag{8}$$

Now let $T_\mathbf{b}$ be a timescale characteristic of $\mathbf{b}$. By dimensional analysis we then have

$$\left|\frac{\partial\mathbf{b}/\partial t}{\eta\nabla^2\mathbf{b}}\right| \approx \frac{R^2}{\eta T_\mathbf{b}} = \frac{T_\eta}{T_\mathbf{b}}\,, \tag{9}$$

where T_η is the timescale of magnetic diffusion (i.e. Ohmic dissipation). Under laboratory conditions for liquid metals T_η is very short compared with $T_\mathbf{b}$. Therefore a *quasistatic approximation*, also known as limit of zero magnetic Prandtl number [15], is justified, with the electromagnetic field evolving through a sequence of steady-state solutions:

$$\nabla^2\mathbf{b} = -\eta^{-1}\nabla\times(\mathbf{v}\times\mathbf{B}_0) \tag{10}$$

On the right of this equation we have also neglected the induced magnetic field, which is small compared with $\mathbf{B}_0$. Equation (10) expresses the quasistatic approximation in a form more general than normally used in liquid-metal studies [8], where not $\mathbf{b}$ but merely, using Ohm's law, $\mathbf{j}$ is calculated and consequently the contribution of $\mathbf{b}$ to the Lorentz force (cf. Sec. 2.2) is neglected.

2.2 Dimensionless equations in cylindrical coordinates

To state the governing equations in a dimensionless form, we first choose a set of units. Let the radius R of the cylinder be the unit of length, the strength j_0 of the imposed current $\mathbf{J}_0$ the unit for the electric current density, and $B_0 = j_0\mu_0 R$ the magnetic field unit, so that $B_0/2$ is the strength of the self-generated part of the equilibrium field (i.e., of the field generated by $\mathbf{J}_0$) at the cylinder mantle. Writing $v_A = B_0/\sqrt{\mu_0\rho}$ for the Alfvén velocity corresponding to B_0, we then normalize $\mathbf{v}$, t, p, and $\mathbf{E}$ (the electric field) by v_A, $\tau_A = R/v_A$, $\rho_0 v_A^2$, and $B_0 v_A$, respectively. The equilibrium magnetic field (4) is given as $\mathbf{B}_0 = (r/2)\mathbf{e}_\varphi$ in the dimensionless form; the external field $\hat{B}\mathbf{e}_z$ is assumed to be zero in the following. With these scalings the evolution equations read

$$\frac{\partial\mathbf{v}}{\partial t} + (\mathbf{v}\cdot\nabla)\mathbf{v} = -\nabla p + \frac{1}{M}\nabla^2\mathbf{v} + \mathbf{J}\times\mathbf{B}\,, \tag{11}$$

$$\nabla^2\mathbf{b} = -S\nabla\times(\mathbf{v}\times\mathbf{B}_0)\,, \tag{12}$$

where $M = v_A R/\nu$ and $S = v_A R/\eta$ are Reynolds-like numbers based on the Alfvén velocity: S is the Lundquist number and M its viscous analogue. The geometric mean of the two Reynolds-like numbers gives the Hartmann number, $Ha = \sqrt{M\,S}$.

Next we write the equations in cylindrical coordinates.

$$\begin{aligned}\frac{\partial v_r}{\partial t} + (\mathbf{v}\cdot\nabla)v_r - \frac{v_\varphi^2}{r} = &-\frac{\partial p}{\partial r} + \frac{1}{M}\left(\nabla^2 v_r - \frac{v_r}{r^2} - \frac{2}{r^2}\frac{\partial v_\varphi}{\partial\varphi}\right)\\ &+(\mathbf{J}\times\mathbf{B})_r \end{aligned}\tag{13}$$

$$\begin{aligned}\frac{\partial v_\varphi}{\partial t} + (\mathbf{v}\cdot\nabla)v_\varphi + \frac{v_r v_\varphi}{r} = &-\frac{1}{r}\frac{\partial p}{\partial\varphi} + \frac{1}{M}\left(\nabla^2 v_\varphi - \frac{v_\varphi}{r^2} + \frac{2}{r^2}\frac{\partial v_r}{\partial\varphi}\right)\\ &+(\mathbf{J}\times\mathbf{B})_\varphi \end{aligned}\tag{14}$$

$$\frac{\partial v_z}{\partial t} + (\mathbf{v}\cdot\nabla)v_z = -\frac{\partial p}{\partial z} + \frac{1}{M}\nabla^2 v_z + (\mathbf{J}\times\mathbf{B})_z \tag{15}$$

According to (1) the Lorentz force splits into four terms:

$$\mathbf{J} \times \mathbf{B} = \mathbf{J}_0 \times \mathbf{B}_0 + \mathbf{j} \times \mathbf{B}_0 + \mathbf{J}_0 \times \mathbf{b} + \mathbf{j} \times \mathbf{b} \tag{16}$$

The first term is the pinch force, which in our case can be balanced by a pressure gradient. It is of order unity in the chosen units. The second and third terms are mixed terms of unperturbed and induced fields and thus of the order Re^M. The fourth term is a product of induced fields and has thus $(Re^M)^2$ as order of magnitude. If the magnetic Reynolds number is much smaller than unity the last term can probably be neglected in the computation. For the three components of the Lorentz force in cylindrical coordinates one gets:

$$(\mathbf{J} \times \mathbf{B})_r = -\frac{r}{2} - j_z \frac{r}{2} - b_\varphi + j_\varphi b_z - j_z b_\varphi \tag{17}$$

$$(\mathbf{J} \times \mathbf{B})_\varphi = \qquad\qquad b_r + j_z b_r - j_r b_z \tag{18}$$

$$(\mathbf{J} \times \mathbf{B})_z = \qquad j_r \frac{r}{2} \qquad + j_r b_\varphi - j_\varphi b_r \tag{19}$$

The above formulae are written such as to have terms belonging to the same summand of (16) in one column above each other. The induced current density is computed from the induced magnetic field, obtained in turn from the vector Poisson equation, Eq. (12), by application of the curl operator in cylindrical coordinates: $\mathbf{j} = \nabla \times \mathbf{b}$. Before coming to the boundary conditions we give the Poisson equations for the magnetic field components in cylindrical coordinates:

$$\nabla^2 b_r - \frac{b_r}{r^2} - \frac{2}{r^2}\frac{\partial b_\varphi}{\partial \varphi} = -\frac{S}{2}\frac{\partial v_r}{\partial \varphi} \tag{20}$$

$$\nabla^2 b_\varphi - \frac{b_\varphi}{r^2} + \frac{2}{r^2}\frac{\partial b_r}{\partial \varphi} = -\frac{S}{2}\frac{\partial v_\varphi}{\partial \varphi} \tag{21}$$

$$\nabla^2 b_z = -\frac{S}{2}\frac{\partial v_z}{\partial \varphi} \tag{22}$$

2.3 Boundary conditions, spectral expansion and timestep

The boundary conditions applied represent a compromise between what one would assume for an experiment and what are necessary simplifications to make a running spectral code sufficiently effective. For the fluid dynamics part we assume no-slip boundary conditions at the cylinder mantle and periodic boundary conitions in the axial direction. The azimuthal coordinate is naturally a periodic coordinate:

$$\mathbf{v}(r = 1, \varphi, z) = 0, \quad \mathbf{v}(r, \varphi, z + h) = \mathbf{v}(r, \varphi, z), \quad \mathbf{v}(r, \varphi + 2\pi, z) = \mathbf{v}(r, \varphi, z) \tag{23}$$

$r = 1$ in our lengthscale corresponds to the radius R of the cylinder; h is the height respectively the periodicity length in dimensionless units, corresponding to a length of $H = hR$. Therefore h is giving the aspect ratio of the cylinder.

Besides the fluid dynamical boundary conditions also electrodynamic boundary conditions have to be imposed for the current density and the magnetic field. We assume nonconducting walls at the cylinder mantle, which means that the component

of the current density normal to the wall has to be zero: $j_r(r = 1, \varphi, z) = 0$. The magnetic field has to satisfy continuity conditions with a solution in the nonconducting exterior of the cylinder, obtained for example by using Biot-Savart's law. This is a managable but cumbersome procedure and we therefore simplify the boundary conditions for the magnetic field by assuming the induced magnetic field to be zero at the cylinder mantle, i.e. $\mathbf{b}(r = 1, \varphi, z) = 0$ [implying $j_r(r = 1, \varphi, z) = 0$].

The boundary conditions allow periodic expansions in the φ and z directions, while in the r direction Chebyshev polynomials will be used. All hydrodynamic and electric variables can be expanded in the following way:

$$\Phi(r, \varphi, z) = \sum_{n=0}^{\infty} \sum_{l=-\infty}^{\infty} \sum_{m=-\infty}^{\infty} \hat{\Phi}^{nlm} T_n(r) e^{il\varphi} e^{im\frac{2\pi}{h}z} \tag{24}$$

Here Φ stands for components of the velocity, the magnetic field, current density or the pressure.

Fourier and Chebyshev expansions have the advantage that one can use fast Fourier transformations (FFTs) to transform arrays from physical space to coefficient space and vice versa. The computation of the nonlinearities can be done in physical space ($\propto N^3$), where it needs much less computation time than in coefficient space ($\propto N^6$). Similarly the computation of the derivatives is much more effective in coefficient space. The FFTs have a computation count $\propto N^3(\log N)^3$. Another advantage of spectral methods is the exponential convergence of the result with increasing number of gridpoints per dimension that sometimes gives high accuracy already for only a few gridpoints (see for example [3]). The timestep can be done in physical space or in coefficient space. For our code we choose to compute the timestep in coefficient space. The nonlinearity and the Lorentz force have to be treated by an explicit method while we can choose an implicit method for the diffusion term of the Navier-Stokes equation. To ensure the incompressibility condition, $\mathrm{div}\mathbf{v} = 0$, we use a fractional step method with solving a Poisson equation for the pressure.

The total timestep in coefficient space —omitting the indices n, l, m— is given as

$$\begin{aligned} \frac{\hat{\mathbf{v}}^{n+1} - \hat{\mathbf{v}}^n}{\Delta t} = &-\nabla \hat{p}^{n+1/2} + \frac{1}{M} \frac{\nabla^2 \hat{\mathbf{v}}^{n+1} + \nabla^2 \hat{\mathbf{v}}^n}{2} - \frac{3\hat{\mathbf{A}}^n - \hat{\mathbf{A}}^{n-1}}{2} \\ &+ \frac{3\hat{\mathbf{F}}^n - \hat{\mathbf{F}}^{n-1}}{2}, \end{aligned} \tag{25}$$

where we have used the abbreviations $\mathbf{A} = (\mathbf{v} \cdot \nabla)\mathbf{v}$ and $\mathbf{F} = \mathbf{J} \times \mathbf{B}$ for the advection term and the Lorentz force, respectively. Here the advection term and the Lorentz force are treated by an Adams-Bashforth scheme of second order while the diffusion term is treated by the Crank-Nicolson scheme, also of second order. This timestep is split in the following way for the application of the projection method (for a more detailed description of the projection method see [13]):

$$\frac{\hat{\mathbf{v}}^* - \hat{\mathbf{v}}^n}{\Delta t} = \frac{1}{M} \frac{\nabla^2 \hat{\mathbf{v}}^n}{2} - \frac{3\hat{\mathbf{A}}^n - \hat{\mathbf{A}}^{n-1}}{2} + \frac{3\hat{\mathbf{F}}^n - \hat{\mathbf{F}}^{n-1}}{2} \tag{26}$$

$$\frac{\hat{\mathbf{v}}^{n+1} - \hat{\mathbf{v}}^*}{\Delta t} = -\nabla \hat{p}^{n+1/2} + \frac{1}{M}\frac{\nabla^2 \hat{\mathbf{v}}^{n+1}}{2} \tag{27}$$

$\mathbf{v}^*$ is an intermediate velocity which is computed in the explicit (first) part of the timestep without the influence of the pressure. The divergence of $\mathbf{v}^*$ is therefore different from zero. The second part of the timestep is implicit. The pressure at step $n + 1/2$ is found by taking the divergence of the equation for the second part of the timestep. To ensure $\nabla \cdot \mathbf{v}^{n+1} = 0$, the pressure has to satisfy the Poisson equation

$$\nabla^2 \hat{p}^{n+1/2} = \frac{\nabla \cdot \mathbf{v}^*}{\Delta t}, \tag{28}$$

which has to be solved before one can calculate the new velocity in the second part of the timestep.

2.4 Spectral Poisson solver

To compute the magnetic field in each timestep and also to compute the pressure in the projection method, a Poisson solver is needed. To preserve the spectral accuracy of the code, the Poisson solver must also be constructed using a spectral expansion. If possible, the operation count for the Poisson solver should be less than that for the FFTs. Otherwise solving the Poisson equation in each timestep would brake the computational velocity of the numerical code. In this section we sketch how this aim can be reached. The needed background on Chebyshev expansions may e.g. be found in [3, 10].

Exemplarily for all four Poisson equations we state the equation for the pressure, $\nabla^2 p = f$, in cylindrical coordinates (multiplied by r^2):

$$r^2 \nabla^2 p = \left\{ \left(r\frac{\partial}{\partial r} \right)^2 + \frac{\partial^2}{\partial \varphi^2} + r^2 \frac{\partial^2}{\partial z^2} \right\} p(r, \varphi, z) = r^2 f(r, \varphi, z) \tag{29}$$

Into the Poisson equation we now insert the (finite) expansion for the pressure used in the spectral code:

$$p(r, \varphi, z) = \sum_{n=0}^{N_r - 1} \sum_{l=-N_\varphi/2}^{N_\varphi/2-1} \sum_{m=-N_z/2}^{N_z/2-1} \hat{p}_{nlm}\, T_n(r) e^{il\varphi}\, e^{ik_m z}, \tag{30}$$

where we have defined $k_m = m(2\pi/h)$. N_r, N_φ and N_z denote the maximum indices after which the expansion is truncated. The expansion functions for the φ and z dependences are eigenfunctions of the corresponding parts of the Laplace operator, but this is not the case with the radial dependence. One gets:

$$\sum_{n=0}^{N_r - 1} \left\{ \left[\left(r\frac{\partial}{\partial r} \right)^2 - l^2 - r^2 k_m^2 \right] \hat{p}_{nlm} - r^2 \hat{f}_{nlm} \right\} T_n(r) = 0 \qquad \forall l, m \tag{31}$$

As we deal with linear operators and because the result of a differential operator applied to a function is again a function that can be expaned in Chebyshev polynomials,

we can consider the following correspondence: A function $\tilde{f}_{lm}(r) =$ (already transformed in the axial and azimuthal directions) has a one to one correspondence to its vector of Chebyshev coefficients $\boldsymbol{f}_{lm} = (\hat{f}_{0lm}, \hat{f}_{1lm}, \ldots \hat{f}_{N_r lm})$ and each operator has consequently a one to one correspondence to a matrix. With the identifications

$$\tilde{Q} \leftrightarrow \left(r\frac{\partial}{\partial r}\right)^2, \qquad \tilde{R} \leftrightarrow r^2 \tag{32}$$

the above equation can be written as the following matrix equation:

$$[\tilde{Q} - l^2 - k_m^2 \tilde{R}]\boldsymbol{p}_{lm} = \tilde{R}\boldsymbol{f}_{lm} \tag{33}$$

Solving the Poisson equation is now reduced to the solution of a linear system of equations with given matrix for each value of l and m. $\tilde{R}$ is a tridiagonal matrix while $\tilde{Q}$ is an upper triangular matrix. Our aim is to have a matrix with only a few diagonals different from zero. Then the solution can be found with $O(N_r)$ operations for each l and each m, which is less than for the Fourier transformation. This aim can be reached by a twofold integration in z, which in our representation is described by a tridiagonal matrix $\tilde{S}$ with elements

$$\tilde{S}_{nj} = \delta_{n-2,j}\,\frac{c_{n-2}}{4(n-1)n} - \delta_{nj}\,\frac{1}{2(n-1)(n+1)} + \delta_{n+2,j}\,\frac{1}{4n(n+1)}, \qquad n \geq 2 \tag{34}$$

where $c_0 = 2$ and $c_n = 1, \forall n \geq 1$. The first two lines of this matrix are equal to zero because each integration is determined only up to a constant. These two zero lines are the proper place to put the boundary conditions for $r = -1$ and $r = 1$. The result is:

$$[\tilde{S}\tilde{Q} - l^2\tilde{S} - k_m^2 \tilde{S}\tilde{R}]\boldsymbol{p}_{lm} = \tilde{S}\tilde{R}\boldsymbol{f}_{lm} \tag{35}$$

One can show that $\tilde{S}\tilde{Q}$ is a tridiagonal matrix (we skip the proof here). $\tilde{S}\tilde{R}$ is the product of two tridiagonal matrices and is itself pentadiagonal. Using a subroutine with a generalized Thomas algorithm one gets an efficient Poisson solver with an operation count less than for the fast Fourier transformations.

3 Results for the sheet pinch using full MHD

3.1 Static Equilibrium

We now allow the magnetic diffusivity η to vary spatially. The induction equation for a uniform η, Eq. (6), has then to be replaced by

$$\frac{\partial \mathbf{B}}{\partial t} = -\nabla \times (\eta\mu_0 \mathbf{J} - \mathbf{v} \times \mathbf{B}), \quad \eta(\mathbf{x}) = \eta_0 \tilde{\eta}(\mathbf{x}), \tag{36}$$

where η_0 is a dimensional constant and $\tilde{\eta}(\mathbf{x})$ a dimensionless function of position.

Using Cartesian coordinates x_1, x_2, x_3, we consider our magnetofluid in the slab $0 < x_1 < L_1$, see Fig. 1. In the x_2 and x_3 directions periodic boundary conditions

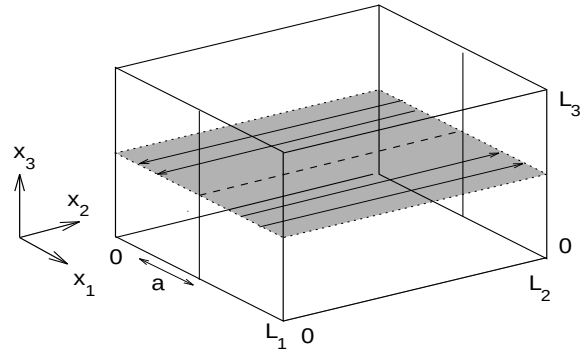

Figure 1 Geometry of the magnetohydrodynamic sheet pinch. Arrows in the shaded plane indicate the direction of the equilibrium magnetic field.

with periods L_2 and L_3, respectively, are used. The boundary planes are assumed to be impenetrable and stress-free, and the system is driven by an electric field in the x_3 direction prescribed on the boundary. We further assume that there is no magnetic flux through the boundary. A detailed discussion of these boundary conditions is found in Ref. [19].

For the case of a uniform η, it is found that the quiescent basic state, in which the current density is uniform and the magnetic field profile across the sheet linear, remains stable, no matter how strong the driving electric field [19]. This contrasts with results of Shan, Montgomery, and Chen [20] for the voltage-driven cylindrical pinch. These authors observed, as an externally applied electric field was raised, transitions first to stationary states with flow and eventually to turbulent states. The situation is reminiscent of the difference between plane and cylindrical hydrodynamic Couette flow: Only for the latter one the basic state becomes unstable.

The quiescent basic state of the sheet pinch can become unstable, however, if η varies across the sheet, due, for instance, to temperature differences between the sheet center and the walls. This results in profiles of the equilibrium magnetic field deviating from linear behaviour. We have studied in detail the Harris equilibrium (an upper index e indicates equilibrium quantities):

$$\tilde{\eta} = \cosh^2[(x_1 - 0.5)/a]\,, \quad \mathbf{J}^e = \left(0, 0, \frac{1}{a \tanh(1/2a) \cosh^2[(x_1 - 0.5)/a]}\right), \tag{37}$$

$$\mathbf{B}^e = \left(0, \frac{\tanh[(x_1 - 0.5)/a]}{\tanh(1/2a)} + \overline{B_2^e}, \overline{B_3^e}\right), \quad p^e = -\frac{\mathbf{B}^{e\,2}}{2} \tag{38}$$

Here a is an effective current sheet half width (the current is strong near the midplane of the sheet and weak near the boundary planes), and all quantities have been made nondimensional as described in Sec. 2.2, now with the distance L_1 between the

boundary planes as the unit of length and the magnetic field strength B_0 on the boundary planes when $\overline{B_2^e} = 0$ (symmetric profile) as the magnetic field unit [18].

3.2 Numerical code

The boundary conditions for the velocity field $\mathbf{v}$ and the induced magnetic field $\mathbf{b}$ read as follows:

$$v_1 = \frac{\partial v_2}{\partial x_1} = \frac{\partial v_3}{\partial x_1} = b_1 = \frac{\partial b_2}{\partial x_1} = \frac{\partial b_3}{\partial x_1} = 0 \quad \text{at } x_1 = 0, 1 \tag{39}$$

Both vector fields are Fourier expanded into modes $\sim \exp\{i(k_2 x_2 + k_3 x_3)\}$ in the x_2 and x_3 directions. In the cross-sheet direction x_1 sine and cosine expansions are used in correspondence with the imposed stress-free boundary conditions (for more details see [19]). Dynamical integrations of the system are performed in Fourier space by means of a pseudo-spectral method with 2/3-rule dealiasing. A Runge-Kutta scheme with a variable time step is used for the time integration. Elimination of the pressure is reached by simple algebraic operations between the Fourier coefficients. The same applies to ensuring $\nabla \cdot \mathbf{v} = 0$ and $\nabla \cdot \mathbf{B} = 0$. No Poisson equation needs to be solved. Thus the planar case with stress-free boundary conditions is computationally much simpler than the cylindrical case with rigid-wall boundary conditions described in Sec. 2.

3.3 Instability

A Squire's theorem could be proven [17] stating that, as M or S are raised, the basic state becomes first unstable to two-dimensional (2D) perturbations, with velocity and magnetic field vectors lying completely in the x_1-x_2 plane and having no x_3 dependence. Furthermore, the instability is nonoscillatory and the stability boundary depends only on the Hartmann number $Ha = \sqrt{M\,S}$ (and not on M and S separately). Figure 2 shows, for $\overline{B_2^e} = 0$ and different values of the Hartmann number, numerically determined stability boundaries in the a-L_2 plane. The unstable region lies to the left of the respective curve. Instability is only possible for $a < 0.4$ [18]; the previously studied case of a spatially uniform resistivity and a linear magnetic field profile [19] corresponds to the limit $a \to \infty$.

The most unstable eigenmode is the 2D tearing mode, which is characterized by a magnetic island structure with a chain of X and O points, fluid motion in the form of convection-like rolls, and a filamentation of the original current sheet, see Fig. 3.

Asymmetry of the configuration with respect to the midplane of the sheet, modelled by a nonvanishing $\overline{B_2^e}$ [cf. Eq. (38)], acts as a stabilizing factor. For $\overline{B_2^e} \geq 1$ there is no reversal of the equilibrium magnetic field within the sheet and the equilibrium is stable.

3.4 Bifurcation

Restricting the whole problem to two spatial dimensions, unstable tearing modes were followed up to a time-asymptotic steady states (see Fig. 4 below, left panel).

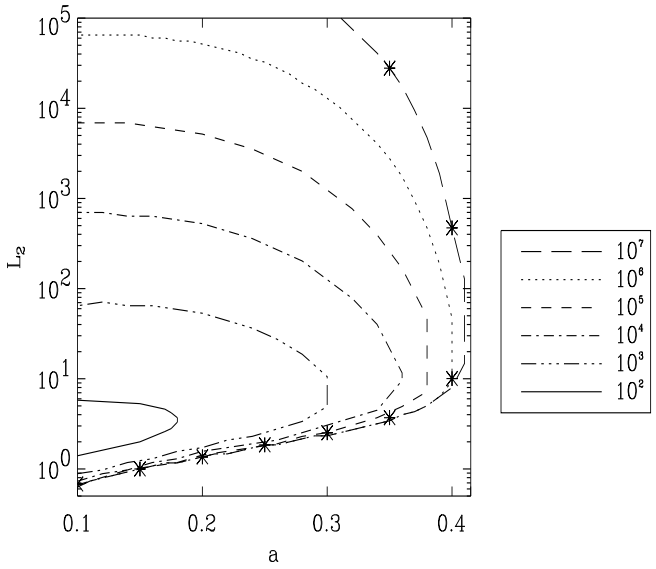

Figure 2 Stability boundaries in the a-L_2 plane for different values of the Hartmann number Ha. The parameter a is the current sheet half width of the equilibrium configuration and $L_2 = 2\pi/k_2$ is the wavelength of the perturbation in the x_2 direction. Asterisks denote calculation with 128 collocation points in the x_1 direction; the other calculations were made with 64 collocation points.

A question coming up then is whether the 2D time-asymptotic states are stable with respect to three-dimensional perturbations. For the case of a spatially uniform resistivity —where all motions must decay in the limit of infinite time— this problem was addressed in numerical studies of the MHD equations by Dahlburg *et al.* [5, 6], who found two-dimensional quasi-equilibria of the tearing-mode type to be unstable to three-dimensional perturbations. These secondary instabilities and their nonlinear development were proposed as a scenario for the transition to MHD turbulence.

We find the time-asymptotic tearing-mode state to be sensitive to three-dimensional (3D) perturbations even close to the point where the primary instability sets in [16]. The instability with respect to 3D perturbations is suppressed by a sufficiently strong magnetic field in the invariant direction of the equilibrium. For a special choice of the parameters, the unstably perturbed state was followed up in its nonlinear evolution and was found to approach a 3D steady state (Fig. 4, right panel).

Although velocity and magnetic field have now components in the invariant direction of the 2D state and are modulated in this direction, there is still some resemblance to the 2D tearing-mode state. This suggest that the unstable 3D perturbations to the 2D state do not drive the system to a completely different solution, but that 2D and 3D solutions originate simultaneously in the primary bifurcation of the basic state. Since our calculations were made very close to the primary bifurcation point, we

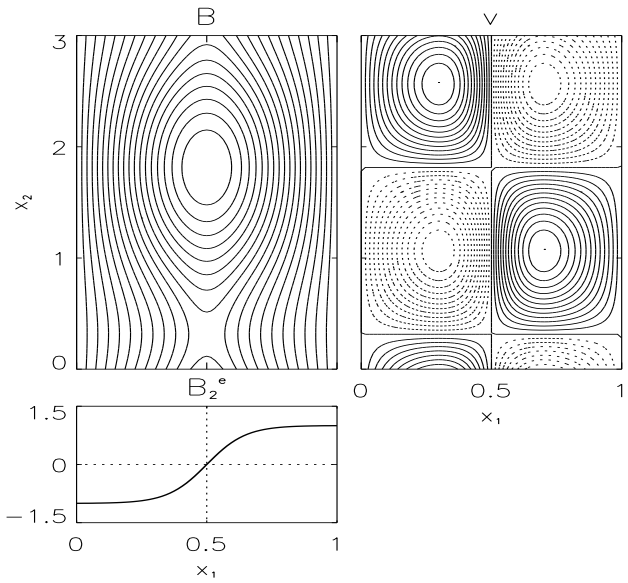

Figure 3 Magnetic field lines and velocity stream lines of an unstable mode for $a = 0.15$, $\overline{B_2^e} = 0$, $L_2 = 3$, and $Ha = 100$. Solid (dashed) velocity stream lines correspond to clockwise (counterclockwise) motion. A mixture of 20% perturbation $\mathbf{b}$ and 80% equilibrium field $\mathbf{B}^e$ was taken for the magnetic field. The lower left panel shows the undisturbed cross-sheet equilibrium profile $B_2^e(x_1)$.

suppose that a supercritical bifurcation leads directly from the basic state to a 3D attractor.

4 Conclusion

Magnetohydrodynamic pinch configurations in cylindrical and planar geometries have been considered. For the cylindrical geometry the appearance of magnetoconvection by the kink instability is known to exist [4, 20]. To investigate the bifurcation sequence starting from this instability for the case of liquid metal inside a cylindrical cavity, the construction of a numerical simulation code based on spectral methods is outlined. To overcome numerical difficulties arising from very different diffusion timescales, expressed by the small magnetic Prandtl numbers of liquid metals ($Pr^M \approx 10^{-5}$), a quasistatic approximation valid for small magnetic Reynolds numbers is applied. After the description of boundary conditions, spectral expansion and the choice of a scheme for the timestep, special attention is paid to the development of an effective spectral Poisson solver. The Poisson solver is necessary to compute the pressure in the fractional timestep of the projection method and also for the determination of the components of the magnetic field in the quasistatic approximation.

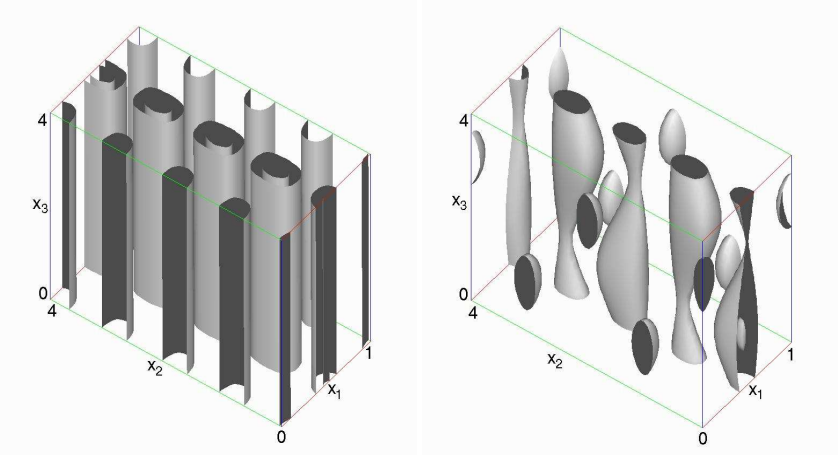

Figure 4 Isosurfaces $|\mathbf{v}| = 0.03$ and $|\mathbf{v}| = 0.016$ for the time-asymptotic 2D state (left) and the time-asymptotic 3D state (right). The values of the parameters are $L_2 = L_3 = 4$, $\overline{B_2^e} = \overline{B_3^e} = 0$, and $Ha = 67.0$. The maximum and minimum values of $|\mathbf{v}|$ are 0.0384 and 0.0017, respectively, in the 2D case and 0.0311 and 0.0, respectively, in the 3D case.

The numerical code for the cylindrical problem is near to completion. Numerical results have already been obtained for a similar problem in planar geometry. The numerical code for the planar case is simpler insofar as no Poisson solver is needed. The pressure can be determined explicitly in Fourier space.

For the case of a uniform electrical conductivity in planar geometry, it is found that the quiescent basic state, in which the current density is uniform and the magnetic field profile across the sheet is linear, remains stable, no matter how strong the driving electric field. Instability is possible, however, for appropriately varying conductivity. We have studied in detail the Harris equilibrium, where the conductivity varies across the sheet in such a way that the current is largely concentrated in a layer centered about the midplane of the sheet and the magnetic field has a hyperbolic-tangent profile. A Squire's theorem could be proven stating that two-dimensional perturbations become unstable first. By varying several parameters of the equilibrium, stability boundaries were determined. The most unstable perturbations are tearing modes, characterized by current filaments, magnetic islands and a fluid motion in convection-like rolls. Restricting the whole problem to two spatial dimensions, the nonlinear evolution of the tearing modes was followed up to time-asymptotic steady states. These proved to be sensitive to three-dimensional perturbations even close to the point where the primary two-dimensional instability sets in. Again stability boundaries were determind, now of the two-dimensional steady tearing-mode states. The instability to three-dimensional perturbations is suppressed by a sufficiently strong magnetic field in the invariant direction of the equilibrium. For a special choice of the system

parameters, the unstably perturbed state was followed up in its nonlinear evolution and was found to approach a three-dimensional steady state.

Acknowledgement

We acknowledge support from the DFG-CNRS German-French research programme 'Numerische Strömungssimulation – Simulation Numérique d'Ecoulements'.

References

[1] G. Bateman. *MHD Instabilities*. MIT Press Cambridge, MA, 1978.
[2] D. Biskamp. *Nonlinear Magnetohydrodynamics*. Cambridge University Press, Cambridge, England, 1993.
[3] C. Canuto, M. Hussaini, A. Quarteroni, T. Zang. *Spectral Methods in Fluid Dynamics*. Springer, Berlin, 1988.
[4] H. Chen, X. Shan, D. Montgomery. Galerkin approximations for dissipative magnetohydrodynamics. *Phys. Rev. A*, 42:6158–6165, 1990.
[5] R. B. Dahlburg. Transition to turbulent electric current sheet reconnection. *J. Plasma Phys.*, 57:35–45, 1997.
[6] R. B. Dahlburg, S. K. Antiochos, and T. A. Zang. Secondary instability in three-dimensional magnetic reconnection. *Phys. Fluids B*, 4:3902–3914, 1992.
[7] R. B. Dahlburg, T. A. Zang, D. Montgomery, and M. Y. Hussaini. Viscous, resistive magnetohydrodynamic stability computed by spectral techniques. *Proc. Natl. Acad. Sci. USA*, 80:5798–5802, 1983.
[8] P. A. Davidson. *An Introduction to Magnetohydrodynamics*. Cambridge University Press, Cambridge, England, 2001.
[9] R. J. Goldston and P. H. Rutherford. *Introduction to Plasma Physics*. Institute of Physics Publishing, Bristol, 1995.
[10] D. Gottlieb, S. Orszag. *Numerical Analysis of Spectral Methods: Theory and Application*. SIAM-CBMS, Philadelphia, 1977.
[11] D. Montgomery. Magnetohydrodynamic stability threshold as a function of Hartmann number and pinch ratio. *Plasma Phys. Control. Fusion*, 34:1157–1162, 1992.
[12] E. F. Northrup. Some newly observed manifestations of forces in the interior of an electric conductor. *Phys. Rev.* 24:474–497, 1907.
[13] R. Peyret, T. Taylor. *Computational Methods for Fluid Flow*. Springer, New York, 1983
[14] E. R. Priest. *Solar Magnetohydrodynamics*. D. Reidel Publishing Company, Dordrecht, 1982.
[15] P. H. Roberts. *An Introduction to Magnetohydrodynamics*. Longmans, London, 1967.
[16] J. Schumacher and N. Seehafer. Bifurcation analysis of the plane sheet pinch. *Phys. Rev. E*, 61:2695–2703, 2000.
[17] N. Seehafer and J. Schumacher. Squire's theorem for the magnetohydrodynamic sheet pinch. *Phys. Plasmas*, 4:4447–4449, 1997.
[18] N. Seehafer and J. Schumacher. Resistivity profile and instability of the plane sheet pinch. *Phys. Plasmas*, 5:2363–2369, 1998.
[19] N. Seehafer, E. Zienicke, and F. Feudel. Absence of magnetohydrodynamic activity in the voltage-driven sheet pinch. *Phys. Rev. E*, 54:2863–2869, 1996.
[20] X. Shan, D. Montgomery, and H. Chen. Nonlinear magnetohydrodynamics by Galerkin-method computation. *Phys. Rev. A*, 44:6800–6818, 1991.
[21] E. Zienicke, A. Thess, B.W. Li, A. Krätzschmar, P.Terhoeven. Stability analysis of the liquid metal pinch using the shallow water approximation. in preparation